Supporting Information for

Measuring the activation energy barrier for the nucleation of single nano-sized vapor bubbles

Jing Chen+, Kai Zhou+, Yongjie Wang, Jia Gao, Tinglian Yuan, Jie Pang, Shu Tang, Hong-Yuan Chen and Wei Wang*

School of Chemistry and Chemical Engineering, State Key Laboratory of Analytical Chemistry for Life Science, Nanjing University, Nanjing 210023, China

+ These authors contributed equally (J. C. and K. Z.)

* To whom correspondence should be addressed. Email: wei.wang@nju.edu.cn

Experimental Methods

Supporting Figures

www.pnas.org/cgi/doi/10.1073/pnas.1903259116

Supporting Movies

Experimental methods

1.1 The SPRM setups combined with optical tweezers system for generation and detection of nano-sized water vapor bubbles

The Surface Plasmon Resonance Microscope (SPRM) setup was built on an inverted total internal reflection fluorescence microscope (Fig. S1) equipped with two decks (TIRFM, Nikon Ti-U). The top deck was used for optical tweezers (see below for details) and the bottom deck was used for SPRM imaging. Gold film with a thickness of 50 nm was coated on a glass coverslip (No. 1 BK7 glass from Fisher) using a magnetron sputter, and served as the substrate for both laser heating and SPRM imaging. The light source used for SPRM imaging was a superluminescent diode (SLED, λ = 680 nm, operating output power 0.1 mW, Qphotonics Inc). The red light is collimated and focused at the back focal plane of a 60× objective with a high numerical aperture (N.A. = 1.49), resulting in a parallel beam of light towards the sample with an adjustable incident angle. The measurement was performed at a fixed incident angle, where the SPR intensity varies linearly with the change

in the refractive index of water. The reflective light is collected by the same objective to produce SPRM images in the CCD camera (Pike F-032, Allied Vision Technology).

The optical tweezers system (Aresis, Tweez 250si) was introduced to focus the continuous-wave near-infrared laser beam (Nd:YAG, λ=1064 nm, spot size 0.87 micron) onto the gold film through the same objective. A short-pass filter (λ < 720 nm) was placed in the microscope filter cube to keep the near-infrared light from entering the CCD camera. The power density of both red light (for SPRM) and near-infrared laser beam (for heating) was detected by a power-meter (PM100D, Thorlabs). A fast camera (Japan, NAC, MEMRECAM GX-8F) was introduced to capture thermal diffusion images at a speed of 100,000 frames per second (time resolution 10 μs). During the experiments of determining the local nucleation rate, a piezo-stage (P-527.2CD, Physik Instrument PI) was used to move the sample stage in x and y directions with an accuracy of 1 nm.

A polydimethylsiloxane (PDMS) cell was placed on top of the gold film-coated coverslip served as the sample chamber, and all researches were performed in deionized water (18.2 MΩ, Smart2Pure 3UF, Thermo Fisher). The deionized water (700 μL) was ultrasonically degassed in a 15 mL centrifuge tube for 30 minutes by ultrasound machine (Fisher, FB15051), filtered twice with Nuclepore Track-Etch Membrane (Whatman, aperture: 50nm), and then added to the sample chamber to form a convex liquid surface protruding the chamber, which was subsequently covered by a glass coverslip to form an approximately closed system by liquid sealing.

1.2 Conversion from SPRM intensity to local temperature (ΔI→ΔT)

The principle of using SPR intensity to calculate the local temperature relied on the dependence of SPR angle on the refractive index of water, which is a function of temperature.

Step 1 (ΔT→Δn): With reference to the refractive index data of water, the correlation between refractive index and temperature of water can be acquired near the wavelength of 680 nm (Index of refraction of water / Handbook of Chemistry and Physics, Eds. Lide D.R., CRC Press LLC, 2000-2001).

Step 2 ($\Delta n \rightarrow \Delta\theta_{SPR}$): SPR angle ($\theta_{SPR}$) has a correlation with the refractive index (n) of

the medium water and *∂θ/∂n* can be obtained through electromagnetic calculation by using opensource software Winspall (developed by Juergen Worm at Max Planck Institute for Polymer Research)..

Step 3 ($\Delta\theta_{SPR}$→ΔI): Through adding 1% ethanol into water, SPR angle change ($\Delta\theta_{SPR}$ = 60 mDeg) can be acquired, which causes the SPR intensity change (ΔI) simultaneously.

Hence we can calculate the temperature change of the water from the experimental measured SPR intensity change using the following equation:

$$\Delta T = \frac{1}{\frac{\partial I}{\partial \theta}\frac{\partial \theta}{\partial n}\frac{\partial n}{\partial T}} \cdot \Delta I \qquad \text{(S1)}$$

The results of *∂θ/∂n*, *∂n/∂T* and *∂I/∂θ* calculated from Fig. S6 and S7 are 129.4 deg· RIU^{-1}, -1.9646×10^{-4} RIU· K^{-1} and 1539 IU· deg^{-1}, respectively, where RIU is refractive index unit. If we define the conversion factor *β* = (*∂θ/∂n*) · (*∂n/∂T*) · (*∂I/∂θ*), then equation (S1) is simplified as

$$\Delta T = \frac{1}{\beta} \cdot \Delta I \qquad \text{(S2)}$$

Using the parameter values of water given above, we have *β* = -39.1 IU·K^{-1}, which allows us to determine local temperature increase relative to room temperature (25℃) from the captured SPRM images.

1.3 Bulk temperature measurement

The schematic apparatus for measurement of bulk temperature is shown in Fig. S5. The thermocouple probe (Gemei) was inserted into the sample chamber containing hot water and then naturally cooled from 47℃ to 30℃. The thermistor output signal, i.e., the temperature display, was synchronized with the SPRM images, exhibiting a decrease in temperature and an increase in SPR intensity over time. Linear fit of the SPR intensity change and the temperature change in Fig. 2*A* gives the slope of -37.4 IU·K^{-1}, which is consistent with the coefficient *β* determined from theoretical calculation mentioned in section 1.2.

1.4 Theoretical analysis of thermal diffusion

The image of the temperature distribution (ΔT) shown in Fig. 2*B* is converted from SPRM image using equation (S2). The temperature at the center of the heating spot is

82.5 K above the room temperature, which decreases rapidly from the center to the surrounding regions, as shown in Fig. S8A (black dots). This temperature distribution is consistent with the thermal diffusion theory mentioned in the article. The theory in brief is that a single spherical gold nanoparticle of radius R_{NP} as the heat source, and the medium surrounding the gold nanoparticle is water just the same as we studied. In the limit t→∞, the temperature distribution outside the nanoparticle is given by a simple formula:

$$\Delta T(\mathrm{r}) = \frac{V_{NP}Q}{4\pi k_0} \cdot \frac{1}{r} \quad (r > R_{NP}) \qquad \text{(S3)}$$

Where k_0 is the thermal conductivity of water, V_{NP} is the volume of the nanoparticle, r is the distance from the surface of the nanoparticle, Q is the local heat generated by the heating light inside the nanoparticle. Here, we use the laser-heated gold film region as an equivalent cylinder nanoparticle. The equivalent gold nanoparticle has a diameter of 0.87 micron, which is the diameter of the heating laser spot, and a height of 50 nm. Hence we applied the formula (S3) to analyze the temperature profile obtained in Fig. S8A (black scattered dots). The fitting result (red line) in Fig. S8A is shown as follows:

$$\Delta T = \frac{465.5}{x+4.469} - 7.466 \qquad \text{(S4)}$$

Where the unit of x is micron.

In terms of the time dynamic of heating, the theory gave an asymptotic formula to describe the relatively fast process:

$$\Delta T(t) = \Delta T_{\max} \cdot \left(1 - \frac{1}{\sqrt{\pi t/\tau_0}}\right) \qquad \text{(S5)}$$

Where τ_0 is a constant related to the radius of nanoparticles with different sizes and $\Delta T_{\max}$ is the temperature at the surface of nanoparticles. The fitting result of Fig. S8B (red line) turned out to be in good agreement with experimental data, and the time constant (27.4 μs) is obtained:

$$\Delta T = 82.5 \times \left(1 - \frac{1}{\sqrt{\pi t/27.4}}\right) \qquad \text{(S6)}$$

Where the unit of t is microsecond.

1.5 Determination of nucleation rate

The periodic on and off time of the heating laser beam was controlled by the program of Tweezer250si. The linear change of the heating laser power was achieved by linear

alteration of the trap strength of the preselected optical trap.

In this work, we first increased the heating laser power from 25.4 mW to 28.5 mW linearly to interrogate the nucleation rate at one position. For each power, 200 cycles of 250 ms heating and 1100 ms recovering processes were performed, measurements at all eight temperatures were repeated for 3 times. Through analyzing the recorded images with MATLAB and ImageJ, the change of temperature, the number of generated nanobubbles and the nucleation time for each power control experiment were acquired automatically.

The histograms of nucleation time under eight different heating powers shown in Fig. 3*B* were converted into the probability distribution of events that do not produce bubbles, $\tilde{P}(t)$, as a function of corresponding heating duration time, *t*. We first assigned the nucleation time into equal time interval and then calculated the probability distribution:

$$\tilde{P}(t) = \frac{N\ (total)\ - N\ (t)}{N\ (total)} \times 100\% \qquad \text{(S7)}$$

Where *t* is the heating duration time, *N* (*t*) is the number of heating events that have nucleation time smaller than *t*, and *N* (*total*) is the number of total heating events. Therefore, *N* (*total*) - *N* (*t*) represents the number of heating events that do not produce bubbles even if the heating duration reached *t*. After obtained the probability distribution versus duration time, an exponential decay equation was introduced as follows:

$$\tilde{P}(t) = exp(-kt) \qquad \text{(S8)}$$

Where *k* is the exponential decay constant represented the first order nucleation rate constant and the unit of *t* is millisecond.

Supporting Figures

2.1 Dual-deck optical configuration consisted of SPRM & optical tweezers

Fig. S1 shows the optical configuration of the apparatus, which consists of a SPRM and an acousto-optic deflector (AOD) scanning optical tweezers system. The SPRM (bottom deck) is used to capture optical images during laser heating modulation. The AOD scanning optical tweezers system (top deck) is introduced to focus a continuous wave laser beam (1064 nm) to locally heat the gold film for producing bubbles. For SPRM imaging, a collimated light beam (with a single wave length 680 nm) is focused on the back focal plane of an oil-immersed objective (with a numerical aperture of 1.49) to achieve parallel

illumination onto a glass coated with 50-nm-thick gold film at a certain incident angle. This incident angle can be adjusted by shifting the focal point on the back focal plane. For optical tweezers system, the laser beam passes through the AOD controlled by computer to achieve beam shifting. Profiting from the AOD, the optical trap position and strength can be arbitrarily controlled just by cursor based on computer soft. However, the trap is set to a fixed position during our research, because the scanning of laser beam with AOD was found to slightly alter the output power at different locations. Then the beam is expanded by beam expander before it is transmitted into the microscope. The expanded beam is coupled into the optical pathway of the microscope by a dichroic mirror after which it is tightly focused onto the gold film using an oil immersion objective lens with Numerical Aperture (NA) of 1.49. After going through a short-pass filter, the reflected light is captured by a CCD camera to produce SPRM images.

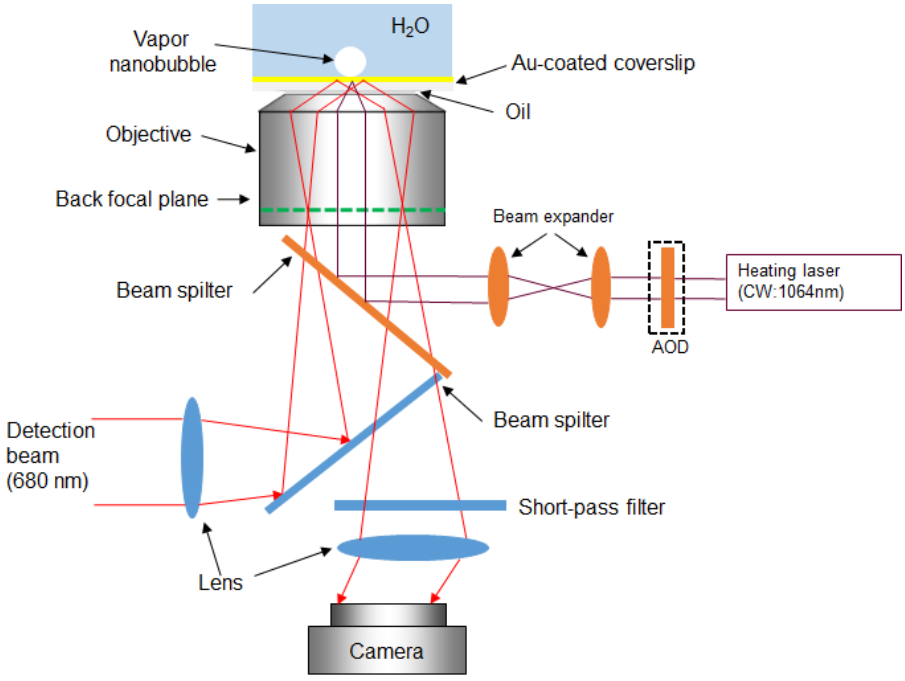

Fig. S1. The optical configuration of SPRM setup combined with AOD scanning optical tweezers system for generation and detection of nano-sized water vapor bubbles.

2.2 Lateral drift-correction system using dual-camera configuration

The dual-camera configuration is shown in Fig. S2A. We used a red superluminescent diode (λ=680 nm, Qphotonics Inc.) as the light source for SPRM imaging. The microscope was also equipped with a green light emission diode (λ=530 nm, M850L2, Thorlabs) for bright-field imaging, which was required for the detection of lateral drift with an accuracy

close to 2 nm by using image correlation analysis. A piezo stage was equipped for x-y drift compensation in real time. As shown in Fig. S2B, the results show that the drift amount in x and y directions were smaller than 5 nm in 2 hours.

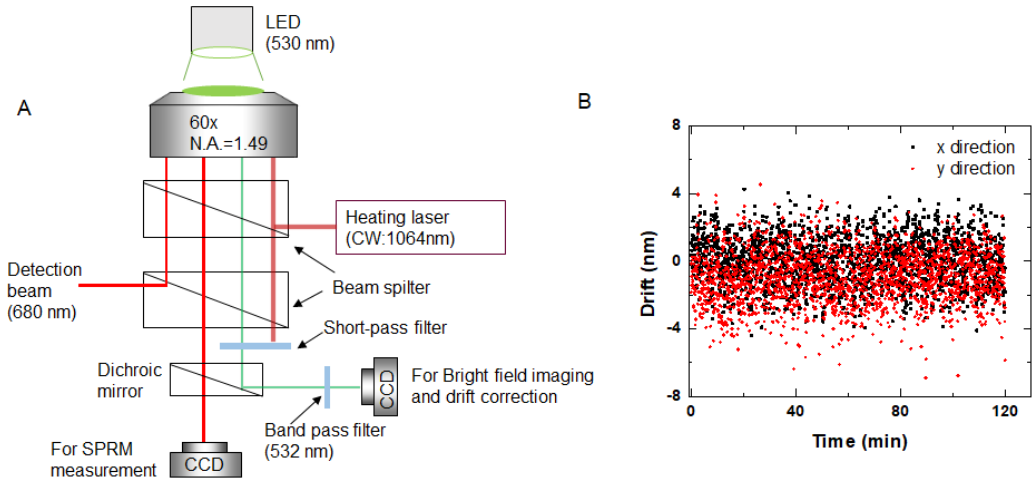

Fig. S2. (A) Schematic illustration on the dual-camera configurations for simultaneous SPRM and bright-field imaging. The latter is required for the detection of lateral drift of sample stage, in order to apply a real-time drift-correction through piezo-stage. (B) Lateral drifts of the sample stage are smaller than 5 nm in 2 hours. Black and red dots represent stability along x and y direction, respectively.

2.3 Nucleation of nanobubbles in early stages revealed by fast camera

In order to track nanobubbles nucleation in the early stage, we utilized a fast camera running at 100,000 frames per second (Japan, NAC, MEMRECAM GX-8F). The time-lapsed SPRM images in the early stage (0-2 ms) of the nucleation are shown in Fig. S3A and the corresponding SPR intensity curve is given in Fig. S3B&C. Note that the thermal effect (round black Gaussian-like pattern) was subtracted to better show the growing behavior of the nanobubble. At 10 μs, a wave-like pattern suddenly appeared in the SPRM image, indicating the formation of a nano-sized bubble within 1 frame. From 10 to 70 μs, the wave pattern became brighter, indicating the continuous growth of the nanobubble.

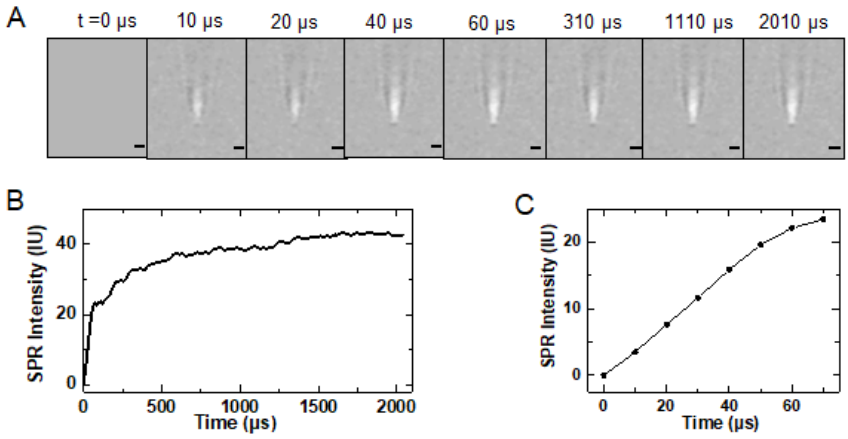

Fig. S3. (A) Snapshots of a nanobubble's formation and growth in the very early stage (0 - 2 ms) by using a fast camera running at 100,000 frames per second. (Scale bar: 2 μm). (B) The corresponding SPR intensity trajectory versus time in the first 2 ms. A zoom-in during 0-70 μs is shown in (C). Note that the fast camera recorded images at a depth of 8 bits. Therefore, the apparent intensity is dozens of times lower than that of the pike camera whose image depth is 14 bits.

2.4 Correlative SPRM and bright-field imaging of the very same nanobubble event

We simultaneously recorded the SPRM and bright-field images for the same individual nanobubbles by using dual-camera configuration (Fig. S2A). Snapshots of both recording are shown in Fig. S4A&B. Comprehensive images can be found in Movie S3. The comparison between SPRM and bright-field images clearly demonstrated the superior sensitivity for SPRM to detect nanobubbles. SPRM was able to identify the appearance of nanobubbles several milliseconds earlier than conventional bright-field microscope. In addition, the image contrast in SPRM is significantly better than that in bright-field images. Both the improved sensitivity and image contrast are critical for more accurate determinations on the nucleation times.

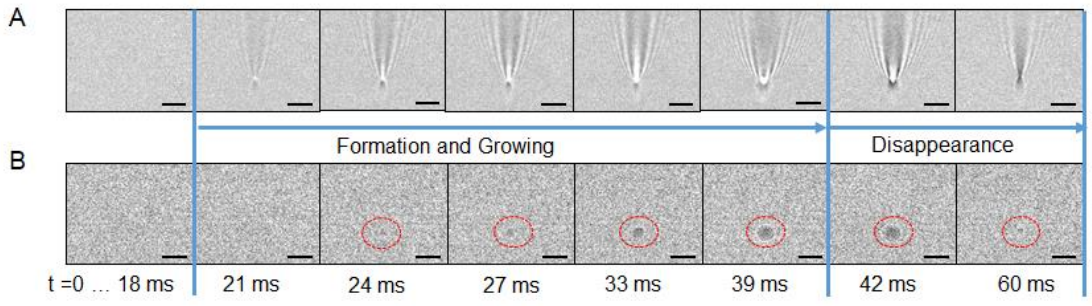

Fig. S4. Simultaneous SPRM (A) and bright-field (B) imaging of the very same single nanobubble event by using two synchronized cameras. The red dotted circle shows the locations of bubble formation. Please refer to Fig. S2 for detailed descriptions on the dual-camera configuration (Scale bar: 5 μm).

2.5 Bulk temperature measurement

In this part, we synchronize the SPRM and a thermocouple to obtain SPR intensity

change and temperature decrease of hot water at the same time. The schematic illustration of the setup is shown in Fig. S5A. After combining the SPR intensity increase and the temperature decrease of hot water, the linear relationship in Fig. 2*A* is obtained.

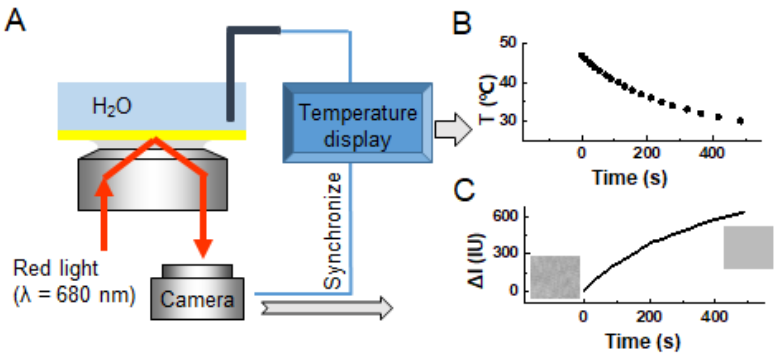

Fig. S5. (A) Schematic illustration of experiment setup for bulk temperature measurement. (B) Temperature decrease of hot water versus time. (C) SPR intensity change during the temperature decrease process. Two inserts show the SPRM images of the beginning (left) and end (right) of the experiment.

2.6 Derivation of parameters ∂θ/∂n and ∂n/∂T for the temperature calculation

(∂θ/∂n): Using Winspall software to simulate different refractive index of medium, the corresponding SPR angle (θ_{SPR}) value is obtained. It is found that the SPR angle and the refractive index are in good linear relationship, and the slope ∂θ/∂n is 129.4 deg·RIU^{-1}.

(∂n/∂T): Referring to the refractive index data of water near the wavelength of 680 nm, the refractive index and temperature of water also have a linear relationship over the temperature range we studied and ∂n/∂T is -1.9527×10^{-4} RIU· K^{-1}.

Fitting results of θ_{SPR}-n, n-T is shown in Fig. S6A &B, respectively.

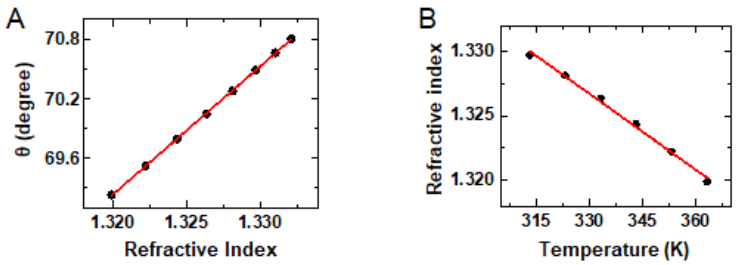

Fig. S6. (A) Surface plasmon resonance angle versus the refractive index of medium from Winspall simulation. (B) Relationship between temperature and refractive index of water.

2.7 Experiment for SPR sensitivity factor ∂I/∂θ

∂I/∂θ is obtained by quantitatively changing ethanol concentration in deionized water and measuring the resulting change in SPR intensity. According to previous experimental result, 1% concentration (V/V) change of ethanol in water increases SPR angle by 60 mdeg.

The increase of SPR intensity along with the change of ethanol concentration (V/V) is shown in Fig. S7A. The starting stage was pure water, then the ethanol concentration in first two steps were both increased by 1 vol%, and that in the third step was increased by 2 vol%. All three steps were considered separately and the average increase in SPR intensity of each stage is obtained. Then in Fig. S7B, we have the linear relationship between ΔI and $\Delta\theta$, as well as the SPR sensitivity factor $\partial I/\partial\theta$, 1539 IU$\cdot \deg^{-1}$

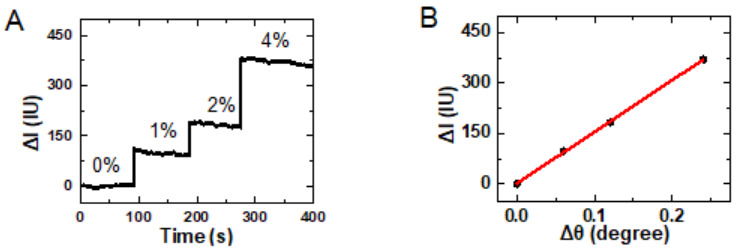

Fig. S7. (A) SPR intensity change varies with ethanol concentration (V/V). (B) The amount of SPR intensity change corresponds to the SPR resonance angle change from (A).

2.8 The thermal diffusion before the generation of vapor nanobubble

The thermal diffusion was further validated by analyzing the spatial distribution of local temperature (Fig. S8A) and temporal dynamics of reaching thermal equilibrium (Fig. S8B). When drawing a straight line across the temperature map shown in Fig. 2*B*, the temperature profile as a function of spatial location is shown in Fig. S8A (black scattered dots). It nicely follows a reciprocal relationship with diffusion distance. Such reciprocal dependence is consisted with the thermal diffusion model. In order to improve the temporal resolution, a fast camera with a frame rate up to 100,000 frames per second was utilized to measure the local temperature change as a function of time (Fig. S8B).

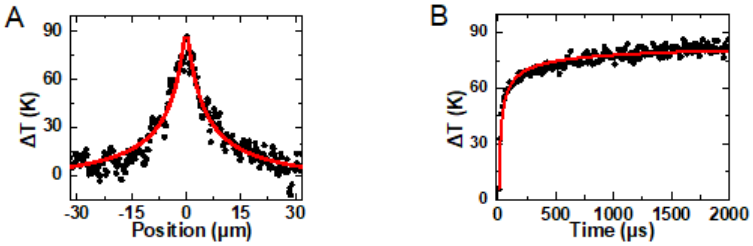

Fig. S8. (A) Spatial distribution of local temperature, the black dots represent spatial profile of temperature along the dashed line shown in Fig. 2*B*, which follows a reciprocal relationship with diffusion distance. (B) Temperature change at the heating spot as a function of time is fitted with theoretical model to access the time constant of thermal equilibrium.

2.9 Nucleation experiment using degassed and air-saturated water

In order to prove that the generated nanobubbles are water vapor nanobubbles rather

than air nanobubbles, the degassed and air-saturated water were utilized to perform the nucleation test at the same position of the gold film, respectively. For both experiments, 200 cycles of laser switching on and off stages were carried out under the laser power of 25.91 mW, with 250 ms heating and 1100 ms recovery time in each cycle. The histograms of the nucleation time distribution for both tests are shown in Fig. S9. As we can see in the histograms, the probabilities of two conditions were close. Further considering the nucleation rate of the bubble generation from the nucleation time histogram, we can see that these two conditions have almost the same nucleation rate constant because the histograms are similar to each other. Thus the nanobubbles that generated both in degassed and air-saturated water were convinced to be water vapor nanobubbles.

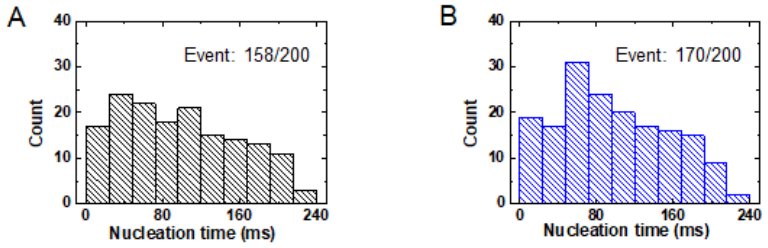

Fig. S9. Histograms of nucleation time distribution. (A) degassed water. (B) air-saturated water.

2.10 Temperature-dependent successful rate of bubble generations

We also studied the correlation between local temperature change (ΔT) versus the heating laser power varying from 24.3 to 27.0 mW (Fig. S10A). The fitting result exhibits a linear relationship. This allows us to verify the local heating temperature measurement under different laser powers with a simple equation:

$$\Delta T = 3.17 \times p + 0.63 \qquad \text{(S9)}$$

Where the unit of p and ΔT is mW and K, respectively.

During the process of linear change with laser power, we observed that there is an obvious increase in the probability of cycles with bubbles as the local heating temperature increased. For each heating power, 200 cycles of laser switching on and off stages were carried out, with 250 ms heating and 1100 ms recovery time in each cycle. This correlation is shown in Fig. S10B, the black dots indicate the values of the experimental statistics, and the red line is the fitting result using the logistic function. This result can be used to predict the probability of cycles with bubbles at different heating temperatures.

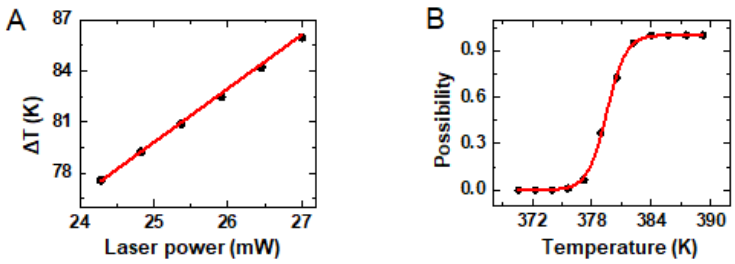

Fig. S10. (A) Linear relationship between heating laser intensity and the measured temperature increase. (B) The correlation between probability of cycles with bubbles and the corresponding heating temperature.

2.11 Automatic identification of the nucleation with computer codes

To automatically identify the appearance of each nanobubble and determine the nucleation time in each cycle, computer codes were written in MATLAB. The SPR intensity curve (Fig. S11A, obtained from Movie S1) was processed with first order derivative method and turned to a more sensitive signal, I_{diff1}, the differential SPR intensity (Fig. S11B), which was used for precise heat and bubble recognition. When heat diffusion (round gaussian like pattern in SPRM images) was detected, i.e., laser switched on, sharp decrease in I_{diff1} was detected. I_{diff1} also provided sharp increase at the moment a nanobubble (wave pattern in SPRM images) was generated. Two thresholds were set to filter the noise of optical signals. During each cycle, the first frame with I_{diff1} < Threshold 1 was automatically recognized by MATLAB program to be the frame that laser switched on. Similarly, the first frame with I_{diff1} > Threshold 2 was considered as the frame with a nanobubble formed.

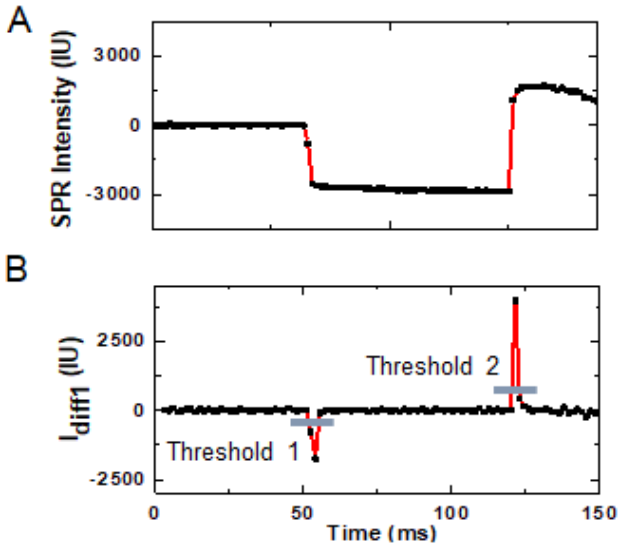

Fig. S11. By identifying the moment of laser application (t_1) and nanobubble formation (t_2) in the SPRM intensity curve (A) with derivative method (B), the nucleation time of each nanobubble (t_2 - t_1) is determined.

2.12 Nucleation rates measurement at different temperatures

The nucleation time required to generate a single vapor nanobubble was found to be highly stochastic in hundreds of bubble generation and collapse cycles. At eight different temperatures, about 200 bubbles were generated at each temperature. The period of each cycle is 1350 ms, consisting of 250 ms heating stage (laser on) and 1100 ms recovery stage (laser off). We repeated the measurements for three times at each data point to examine the reproducibility. The nucleation rate of nanobubbles at each temperature was obtained among all three measurements, which were shown in Fig. S12.

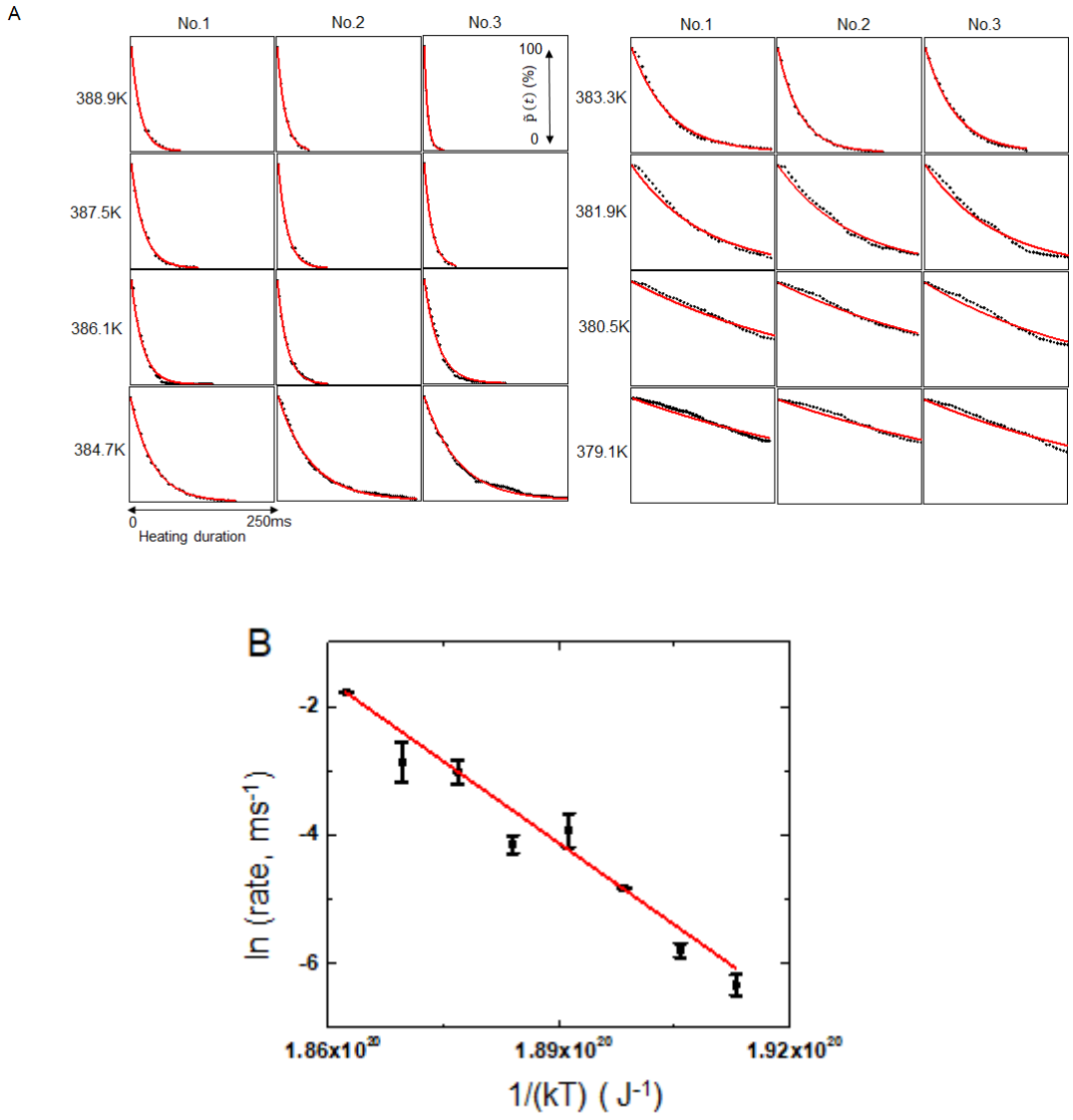

Fig. S12. (A) Fitting the probability as a function of time with mono-exponential function rate under eight temperatures in the very same position for 3 repeated experiments. (B) Average of three measurement leads to a curve containing eight data points with error bars.

2.13 Mapping the nucleation rate with 1-micron resolution

We applied a piezo-stage to move the sample stage one micron each time with an accuracy of 10 nm and determined the nucleation rate at different position under the same heating power, i.e., the same temperature. In specific, experiments were carried out in an area of 5 x 5 μm^2 on the gold film, which was pre-marked outside for the following AFM test. This area was equally divided into 25 regions by scanning the sample stage, each zone is 1 micron apart and the heating laser is focused at its center. For each region, 100 cycles of laser switching on and off stages were carried out under the laser power of 27.50 mW, with 50 ms heating and 2000 ms recovery time in each cycle. Due to the increase in heating laser power, we reduced the heating time to suppress bubble growth and the recovery time required in each cycle. The exponential fitting results on the basis of classical nucleation theory for all 25 locations are shown in Fig. S13, which indicates that the nucleation rate is very different at adjacent locations at distances of a few microns.

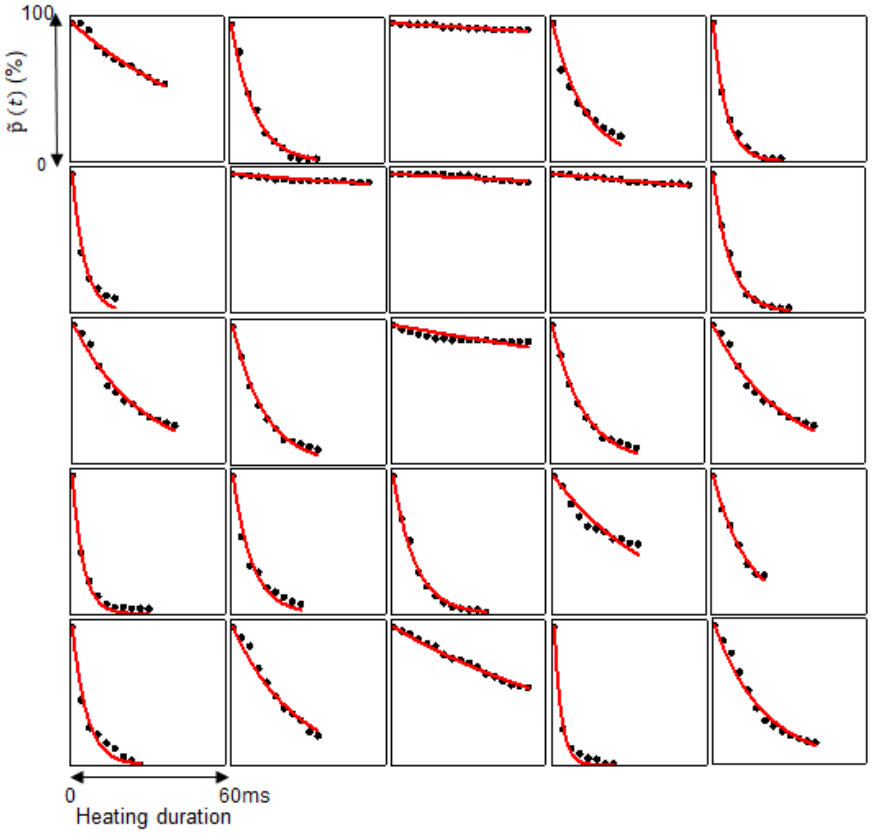

Fig. S13. The probability distribution at all 25 segments. Rate constants from each segment were extracted to generate the map of nucleation rate shown in Fig. 4*A*.

2.14 Super-localization of nucleation sites of nanobubbles

Super-localization of each nanobubbles in 400 continuous cycles revealed a much

narrower distribution of the nucleation site in a range of 80×500 nm^2. The localization accuracy along x-direction was six times better than that along y-direction because of the parabolic tails along the propagation direction (y) of surface plasmon polaritons. Further fitting of the histograms of sites in x and y direction exhibited normal distributions, which are consistent with the Gaussian-like spatial distribution of beam intensity.

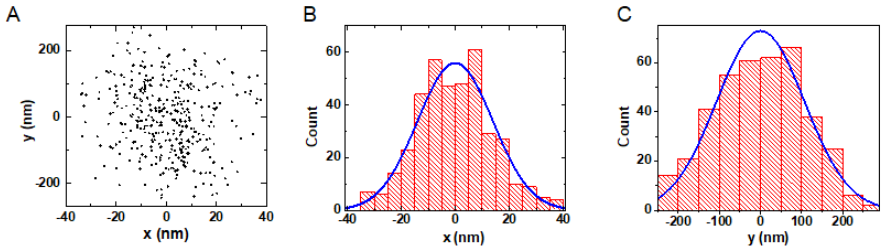

Fig. S14. (A) Super-localization of the nucleation sites of each nanobubble during 400 consecutive cycles. (B) and (C) Histograms of sites in the x and y directions follow normal distributions.

2.15 Nucleation rate regulation by surface chemistry

In order to demonstrate how surface chemistry affected the nucleation rate, we measured the nucleation rates of the very same location by altering its oxidation states with electrochemical oxidation and reduction. Specifically, the nucleation rate was determined to be 0.04837 ms^{-1} on the gold film in its initial state (Fig. S15A). Then a +600 mV potential (vs Ag/AgCl) was applied for 70 seconds to partially oxidize the gold substrate, which changed the surface chemistry. Nucleation rate was determined to be 0.02304 ms^{-1} after this oxidation process (Fig. S15B), which was 53% smaller than its original value. Last, a -600 mV potential was applied for another 70 seconds to reduce the gold substrate. The nucleation rate was found to be recovered (Fig. S15C, 0.05124 ms^{-1}).

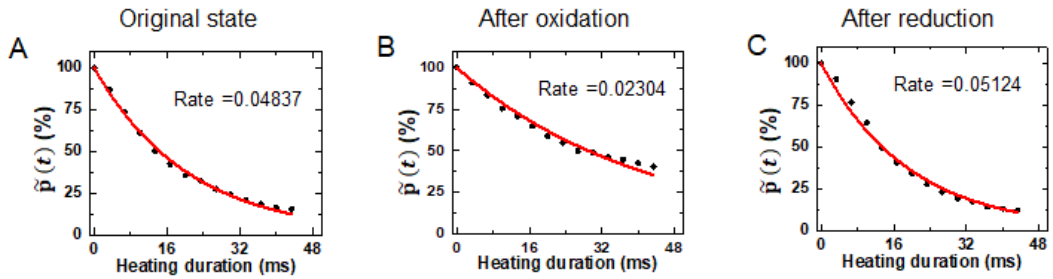

Fig. S15. Nucleation rate of the same location at the original state (A), after electrochemical oxidation (B) and subsequent reduction (C). During each measurement, 200 consecutive cycles were examined under the same laser power.

Other Supporting Information

3.1 Movie S1

Movie S1: Real-time images of a typical process of a water vapor nanobubble's nucleation, growth and dissolution, from which some specific snapshots shown in Fig. 1*C* is extracted. The first SPRM image is subtracted in Movie S1 to better display the relative change in the local refractive index. Note that the nucleation position does not overlap with the optical center of dark shadow in SPRM image due to the propagation of SPPs (upwards herein).

3.2 Movie S2

Movie S2: Real-time images of 10 cycles of heating laser switching on and off stages under the laser power of 25.91 mW (380.5 K), with 250 ms heating and 1100 ms recovery time in each cycle. The first SPRM image is subtracted in Movie S2 to better display the relative change in the local refractive index.

3.3 Movie S3

Movie S3: Real-time images of 5 cycles of heating laser switching on and off stages, with 40 ms heating and 330 ms recovery time in each cycle. The first SPRM and bright-field images are both subtracted in Movie S3 to better display the relative change in the local refractive index.